Research in Astronomy and Astrophysics, 23:065011 (18pp), 2023 June https://doi.org/10.1088/1674-4527/accc75

Lyα Emission Enhancement Associated with Soft X-Ray Microflares

Zheng-Yuan Tian[1,2], Li Feng[1], Lei Lu[1], Fan-Xiaoyu Xia[1,2], Yang Su[1], Wei-Qun Gan[1], Hui Li[1], and Yue Zhou[1,2]
[1] Key Laboratory of Dark Matter and Space Astronomy, Purple Mountain Observatory, Chinese Academy of Sciences, Nanjing 210023, China; lfeng@pmo.ac.cn, leilu@pmo.ac.cn
[2] School of Astronomy and Space Science, University of Science and Technology of China, Hefei 230026, China
Received 2023 February 28; revised 2023 March 26; accepted 2023 March 29; published 2023 May 17

Abstract

Lyα (Lyα, 1216 Å) is the strongest emission line in the solar ultraviolet spectrum. In the present work, we obtained a Lyα enhancement catalog covering flares larger than B1 class from the GOES/EUVS data during 2010–2016. We focused on the 242 B-class events which are less investigated, however, show non-negligible Lyα emission enhancement. We found that on average the Lyα peak of B-class flares is 0.85% stronger than the background. For the flare energetics, it is found that the weaker the soft X-ray (SXR) flare, the larger the ratio of the radiated energy in Lyα to SXR. Using the RHESSI data and multi-wavelength observations taken by SDO-AIA, we diagnose the thermal and non-thermal properties of several flares. Three case studies show that the coincidence of the Lyα peak with the SXR time-derivative peak is not a sufficient condition of the nonthermal property of a Lyα microflare. The Lyα enhancement in the microflares may be caused by the nonthermal electron beams or/and thermal conduction. However for type III events, we found that the delay of the Lyα peak with respect to the SXR peak can be attributed to either the Lyα emission from a filament erupted or the cooling of the thermal plasma in flare loops. Furthermore, interestingly the Lyα emission from filaments can not only occur in the decay phase of the flare, but also in the pre-flare phase. In this case, the Lyα emission was originated from an erupted filament which probably initiated the flare.

Key words: Sun: flares – Sun: chromosphere – Sun: UV radiation – Sun: filaments – prominences

1. Introduction

The line of neutral hydrogen Lyα (Lyα) at 1216 Å is the brightest emission line in the solar UV spectrum (Curdt et al. 2001), early studies showed that during flare occurrence, the spectral line of Lyα shows obvious radiation enhancement (Woods et al. 2004; Rubio da Costa et al. 2009; Milligan et al. 2012). The emission of this line may have a strong impact on the ionosphere of the Earth and space environment. However, due to limited solar observations in Lyα, we have not much understanding of the physical origin of Lyα emissions in solar flares.

For large flares, there has been some statistical work to study the Lyα emission of these flares. Milligan et al. (2020) made a statistical study on 477 M-class and X-class flares observed by the E-channel centered on the Lyα line of the Extreme Ultra-Violet Sensor (EUVS) on board the Geostationary Operational Environmental Satellites (GOES). The results showed that majority of the flares (about 95%) produced less than 10% higher Lyα emission than the background, and the maximum enhancement in all flares is about 30%. They also measured the total radiated energy in Lyα and in soft X-ray (SXR) from 1 to 8 Å, and found that the energy in Lyα is 1–2 orders of magnitude higher than that in the 1–8 Å SXR.

Milligan (2021) carried out the superposed-epoch analysis of the time series of the 453 M- and 31 X-class flares, which resulted in a 1%–4% increase in Lyα emission. Jing et al. (2020) had also detailed statistical work on M- and X-class flares observed by the GOES during 2006–2016, including the duration, location, and peak fluxes of flares. Based on the time difference between the Lyα peak and SXR 1–8 Å peak, they categorized the M- and X-class flares into three types. They found that the three types appeared to have no dependence on the flare duration, flare location, or solar cycle.

Regarding the physical origin of the Lyα emission in solar flares, large flares obviously get more attention. The non-thermal origin of Lyα from the accelerated electrons has been illustrated in previous studies (Nusinov et al. 2006; Rubio da Costa et al. 2009; Dominique et al. 2018). The type I flares had earlier Lyα peak than the 1–8 Å peak, which may follow the Neupert effect (Jing et al. 2020). Therefore, such Lyα emission might be generally related to nonthermal electron beam heating (Nusinov et al. 2006; Milligan & Chamberlin 2016; Chamberlin et al. 2018). However, their type III flares had a delayed Lyα peak than the 1–8 Å peak, which perhaps had a thermal origin from the flare loop cooling. Their simulation revealed that the delay time between the emissions at different wavelengths from high to low temperatures was consistent with the plasma cooing in flare loops, which was related to the flare heating magnitude and especially the flare loop length (Jing et al. 2020).

There are some observations and statistics indicating that the eruption of filaments can also produce significant Lyα emissions. Rubio da Costa et al. (2009) observed the Lyα emission of the failed-erupting filaments, it was found that the heated filament material still had enough neutral hydrogen to scatter the ultraviolet flare radiation from the chromosphere. Milligan (2021) observed a C6.6 flare and found a high increase in Lyα of 7%, which may be attributed to the failed filament eruption. Most recently, Wauters et al. (2022) found that a late-phase peak of the Lyα emission after the main flare peak was correlated with the timing of a filament eruption.

However, most of the previous work focused on the characteristics of the Lyα emission of M-class and X-class flares. Several studies reveal that some microflares exhibit high temperature/non-thermal emissions in roughly the same ratio as large events (Hannah et al. 2008, 2011). As reported by Glesener et al. (2020), even an A5.7-class microflare can be nonthermal as evidenced by the nonthermal hard X-Ray (HXR) emission using direct-focusing NuSTAR observations. The research of an A-class microflare by Li et al. (2022) show the existence of a nonthermal component down to 6.5 keV, indicating that accelerated electrons play an important role in microflares, as in large flares.

There were few studies on the Lyα emissions of microflares. Lu et al. (2021) devised an automatic flare detection algorithm and produced a Lyα flare catalog between 2010 April 8 and 2016 June 6 covering flares larger than B1 class. Their frequency distributions of the peak flux and the fluence of Lyα flares, implied that more flares can accumulate at small scales and these small-scale events play an important role in explaining the energy release in the Sun. Milligan (2021) applied the superposed epoch method to 3123 B-class and 4972 C-class flares. The results showed that for B-class flares they produced a 0.1%–0.3% enhancement above the background Lyα irradiance on average. The average Lyα peak coincided with the SXR peak for the summed B-class flares. It was found that the Lyα emissions from B-class flares may be thermally generated, while C-, M-, and X-class flares exhibit more nonthermal Lyα emissions.

Taking advantage of the Lyα flare catalog built by Lu et al. (2021), we are able to retrieve the light curves of 242 individual GOES B-class flares with visible Lyα irradiance enhancement above the background. Although the number of detected B-class flares is much smaller than the 3123 B-class flares used in Milligan (2021), we do not rely on the superposed epoch technique to increase the flare signal, and the 242 B-class flares are sufficient for statistics. Therefore, we are aiming at making statistical and case studies of these B-class Lyα flares, and investigating whether the thermal and nonthermal properties of individual B-class Lyα flares can deviate from their average properties, e.g., their Lyα emissions are thermally generated from the superposed epoch analysis. It is also pointed by Milligan (2021) that individual events can sometimes skew the average results.

In addition, much of the previous work on Lyα emission of events was based on the start time and end time of the GOES SXR flare list. In fact, this may not be consistent with the actual start and end times of the Lyα emission, which may influence flare properties, e.g., the radiated energy in Lyα, especially for small events. In Lu et al. (2021), we determined the start and end times of the Lyα emission based on the light curve of the Lyα emission itself. Therefore, these two times are more precisely derived.

In this work we selected the Lyα events from the aforementioned catalog, which are also marked as B-class events in the GOES SXR flare list. A threshold of the Lyα emission was set to exclude those events whose Lyα irradiance enhancement cannot be clearly identified by human eyes. In Sections 2 and 3, we describe the data set and the relevant observations by a few instruments that we use. In Section 4, we present the statistical analysis of the chosen B-class Lyα flares. Similar to Jing et al. (2020), we divided the Lyα events set into three types and compared the statistics of B-class flares with larger M- and X- flares. Section 5 is dedicated to the thermal and nonthermal properties of type I Lyα flares, an interesting type I event whose Lyα peak is before its corresponding SXR time-derivative peak. Section 6 provides different interpretations of the delay of Lyα peaks with respect to the corresponding SXR peak for type III events. Conclusions and outlook are given in Section 7.

2. Instruments and Observations

The Lyα irradiance and the SXR (1–8 Å) fluxes used in the present study were measured by the EUVS (Viereck et al. 2007) and the X-ray Sensor (XRS, Hanser & Sellers 1996) both on board the GOES, respectively. The EUVS is dedicated to measure the solar irradiance at a time cadence of 10.24 s in five EUV channels between 50 and 1270 Å, namely, A, B, C, D, and E, with the E-channel targeting on the Lyα emission at 1216 Å, while the XRS is used to characterize the solar SXR fluxes in 0.5–4 Å and 1–8 Å with a time cadence of 2 s. Both measurements have been calibrated into the standard flux unit of W m^{-2}.

Imaging observations from the Atmospheric Imaging Assembly (AIA, Lemen et al. 2012) on board the Solar Dynamics Observatory (SDO) are used to locate the flares. AIA provides images of the solar disk and the low corona in seven EUV wave bands (94 Å, 131 Å, 171 Å, 193 Å, 211 Å, 304 Å and 335 Å) with a time cadence of 12 s and two UV wave bands (1600 Å and 1700 Å) with a cadence of 24 s.

Finally, the Reuven Ramaty High Energy Solar Spectroscopic Imager (RHESSI, Lin et al. 2002) observes solar X-rays and gamma-rays from 3 keV to 17 MeV and has the capability to separate the main thermal emissions from nonthermal

Table 1
A Lyα Emission Enhancement Catalog between 2010 April 8 and 2016 June 6 Associated with B-class SXR Flares (Partially Shown)

N: flare index
Date: day of observation
Start: Lyα enhancement start time (UT)
Peak: Lyα enhancement peak time (UT)
End: Lyα enhancement end time (UT)
Dur: duration of event in unit of minute
Startf: initial Lyα emission in unit of 10^{-3} W m^{-2}
Peakf: peak Lyα emission in unit of 10^{-3} W m^{-2}
Endf: end Lyα emission in unit of 10^{-3} W m^{-2}
Signif: peak flux increase relative to the greater value of start/end fluxes, in %
Class: the GOES class of the SXR flare
Postscript: A means concurrent filament/jet, B means multiple source regions

#N	Date	Start	Peak	End	Dur(m)	Startf	Peakf	Endf	Signif(%)	Class	Postscript
…											
82	2012-8-23	05:21:49	05:30:56	05:43:19	21.5	7.1357	7.2227	7.1357	1.2196	B2.8	B
83	2012-9-13	01:07:26	01:23:28	01:36:22	28.9	6.8234	6.9508	6.8453	1.5418	B6.5	
84	2012-9-15	23:31:10	23:39:34	23:56:07	25	6.8706	6.9325	6.8706	0.9009	B4.2	
85	2012-9-19	05:45:52	05:48:46	06:04:03	18.2	7.2134	7.2644	7.1843	0.7072	B5.3	
86	2012-12-3	11:32:07	11:35:01	11:49:46	17.6	7.3294	7.3663	7.3183	0.5037	B3.9	
87	2012-12-8	10:08:33	10:15:28	10:16:56	8.4	7.3909	7.5017	7.4611	0.5446	B2.9	
88	2012-12-8	10:17:29	10:18:55	10:30:23	12.9	7.4463	7.5128	7.4389	0.893	B8.4	
89	2012-12-21	06:07:15	06:12:53	06:25:59	18.7	7.74	7.84	7.7363	1.2915	B6.8	A
90	2012-12-22	01:27:03	01:30:30	01:32:51	5.8	7.7189	7.767	7.7189	0.6236	B6.8	A
91	2012-12-27	05:08:13	05:21:42	05:31:22	23.1	7.5069	7.5699	7.5217	0.6404	B4.4	A
92	2012-12-30	05:50:10	05:54:11	05:56:43	6.6	7.5181	7.6034	7.5552	0.6379	B3.7	
…											

emissions at higher energies with the technique of imaging spectroscopy (Hurford et al. 2002). It thus can provide diagnostics of energetic electrons in solar flares.

3. The Event List

In the paper by Lu et al. (2021), a Lyα flare list with a total number of 2038 during the time range from 2010 April 9 to 2016 June 6 was generated with an automatic flare detection method. This flare list gives the start, peak, and end times/fluxes, as well as the significance of each Lyα event. The significance index is defined as the ratio of the excess peak Lyα flux relative to the background value, and the greater value of the Lyα event start and end fluxes is used as the background value, which is different from that of Milligan et al. (2020), their background value is a constant fitted with a 24 hr period.

However, the flare list included only flares with significance values larger than or equal to 0.8%, thus misses some small events. In the present work, we reduce the offset significance value to 0.5% and consider only events also associated with SXR enhancements, which forms an event list with a total number of 2068. According to the GOES 1–8 Å peak flux, the event list involves 33 X flares, 365 M flares, 1428 C flares and 242 B flares.

Here we focus primarily on the B-class flares. Similar to Jing et al. (2020), these flares were also divided into three types, with type I/III characterized by a Lyα peak time earlier/later than that in SXR emission, and type II characterized by the similar peak times in Lyα and SXR emissions. Among the 242 B-class flares there are 118 (∼48.76%) type I events, 35 (∼14.46%) type II events and 89 (∼36.78%) type III events. Table 1 shows a portion of this Lyα emission enhancement catalog. In general, the Lyα peak time of type I flares is often close to the derivative peak time of SXR emission, showing Neubert effect, which is considered to be nonthermal flares, while type III flares are often considered to be thermal.

It is worth noting that for these weak events, there may be other processes on the solar disk that could be responsible for the increase of Lyα emission (e.g., a jet, filament eruption, or active region development). To confirm whether the filament/jet bursts affect the distribution of Lyα radiated energy in B-class events (as shown in Figure 4), we examined the AIA images at 304 Å for 242 events and found that approximately 74 flare events were accompanied by filament eruption or jets, accounting for approximately one-third of the total number of events. The enhancement of the Lyα emission of these events may be contributed by both flares and eruptive filaments. They usually take place in the same event. We record them as A in Postscript of Table 1, which means concurrent filament/jet.

There are also cases that multiple source regions could be responsible for the same Lyα emission enhancement, we record them as B in Postscript of Table 1. We found that such cases are about 5% of the total number of events in Table 1. These

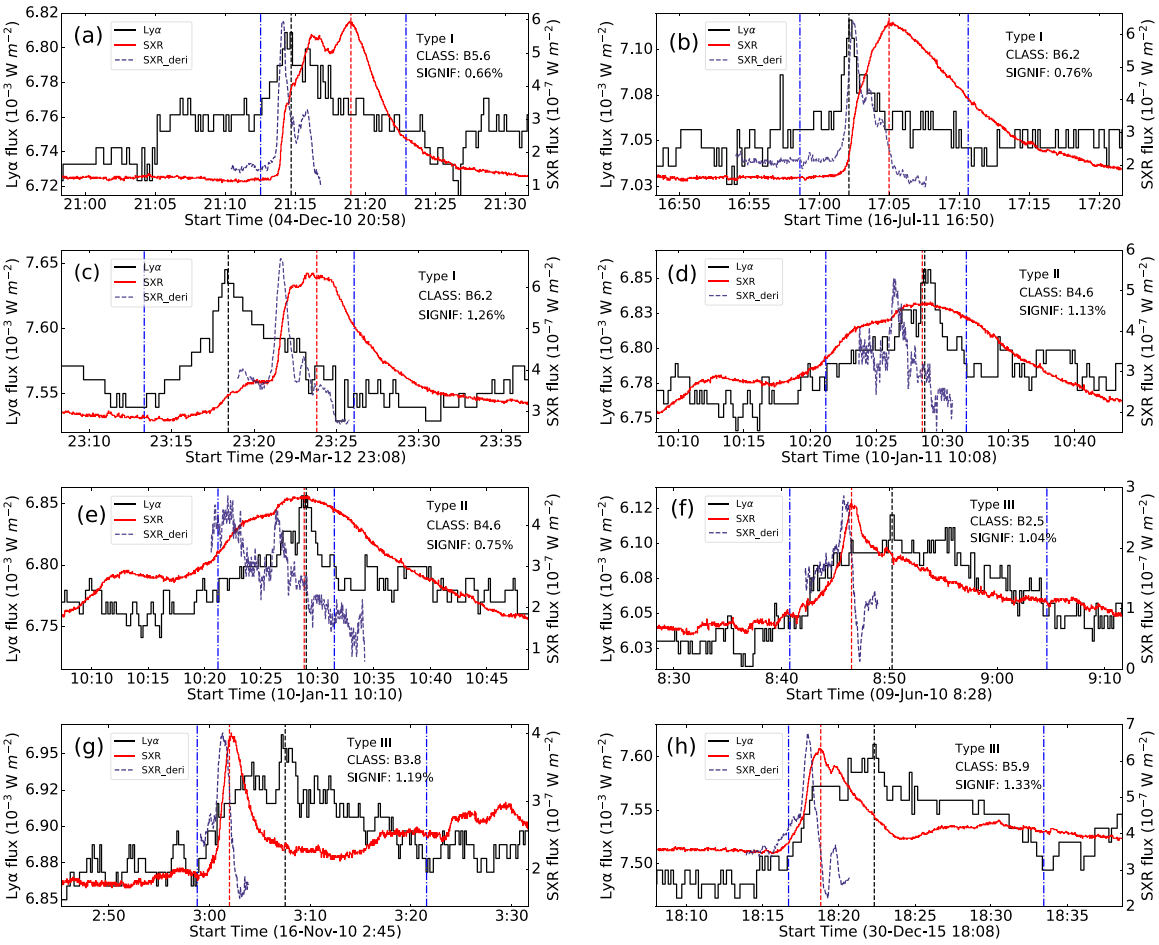

Figure 1. Some typical light curves for the type I (a)–(c), type II (d), (e), and type III (f)–(h) events with the significance index greater than 0.5%. Their significance index, flare class and type are marked in the top right corner of each panel. The black curve marks the Lyα flux corresponding to the left coordinate. The red curve represents the 1–8 Å SXR flux, corresponding to the right coordinate. The blue dashed curve represents the time derivative of the smoothed SXR flux. The red and black vertical dashed lines mark the peak time of SXR and Lyα emission, respectively. The blue vertical lines denote the start and end time of Lyα emission.

events account for a very small proportion and do not affect the statistics and calculation results in our paper.

Figure 1 shows a few examples of the sampled events, including three type I events (Figures 1(a)–(c)), two type II events (Figures 1(d)–(e)) and three type III events (Figures 1(f)–(h)). As can be seen, even in the GOES B-class flares, the Lyα emission can be significantly enhanced. Below we carry out the statistical and case studies of these events.

4. Statistical Analysis of B-class Lyα Events

4.1. Time Properties

Figure 2(a) shows the distribution histogram of the 242 B-class events over years, overplotted with the total number of sunspots in each year. It was found that the occurrence of B-class flares does not seem to correlate with the total number of sunspots, especially in 2014, which have the most sunspots but fewer B-class flares. This is different from the statistical result for M- and X-class flares (Jing et al. 2020).

Figures 2(b) and (c) show histograms of the flare duration (difference between the flare start and end times) in Lyα and SXR, respectively. As can be seen, the duration of the SXR flares ($\sim$14 minutes on average) are systematically shorter than the duration of Lyα flares ($\sim$18 minutes on average). This is likely due to the different methods used to determine the flare start and end times. For the Lyα events, both their start and end times are strictly determined with the improved flare detection algorithm described in Lu et al. (2021), while for the SXR flares, a flare is thought as having ended once the SXR flux drops to a value halfway from the flare peak to its start level. Previous studies usually use the timing of the SXR flares as an estimate for the timing of the Lyα flares, which could somehow result in some systematical underestimation of the flare physical properties such as the flare fluence and energetics.

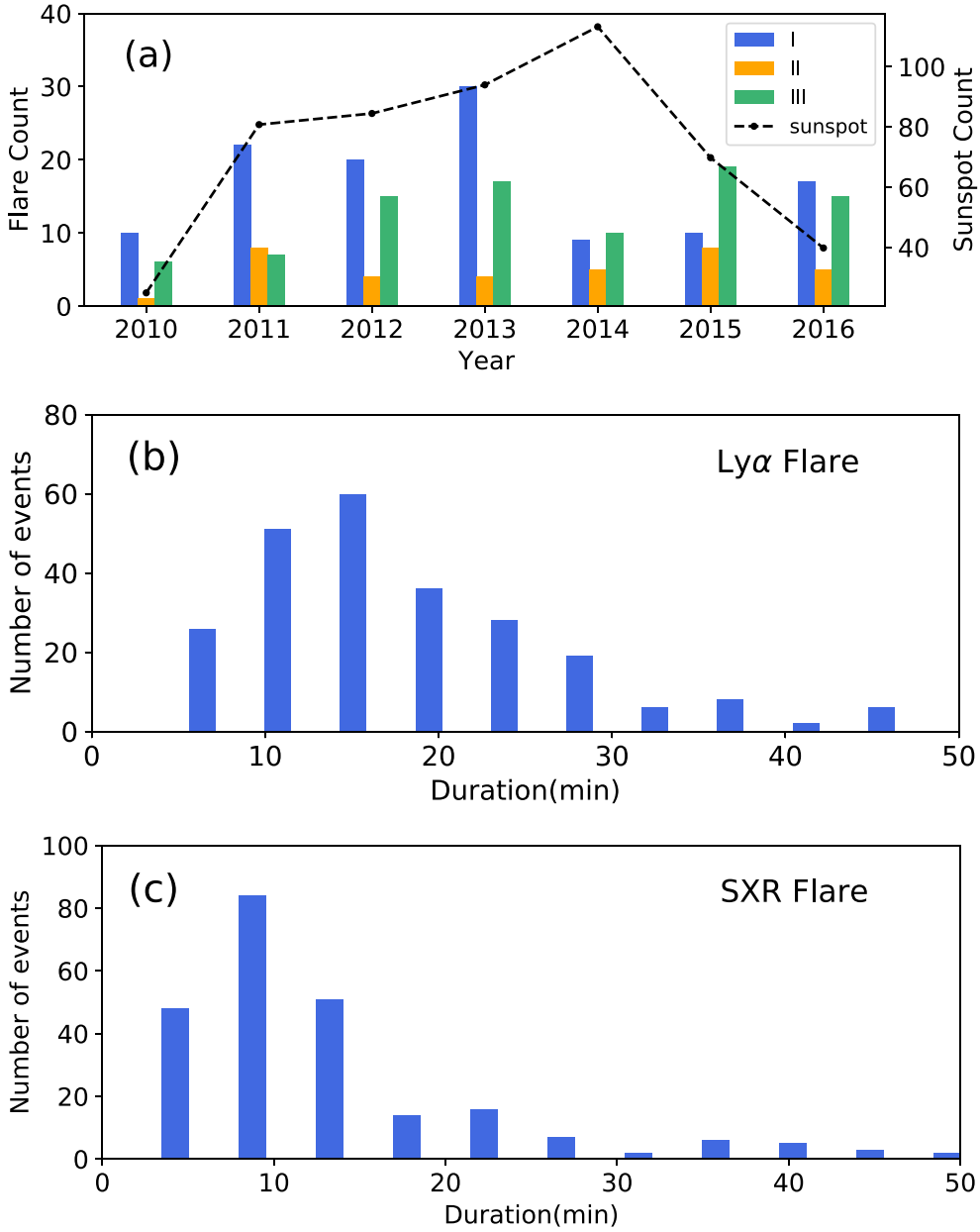

Figure 2. (a) The distribution histogram of the 242 B-class events over years, overplotted with the counts of sunspots at the period of 2010–2016. The blue, yellow, and green colors represent the type I, type II, and type III B-class events, respectively. (b), (c) Histograms of the flare duration (difference between the flare start and end times) in Lyα and SXR, respectively.

To improve the flare signal and reduce background fluctuations, the Lyα time profiles associated with the 242 GOES B-class flares was aligned and averaged using the SXR peak times as a fiducial time, shown in Figure 3(a). As can be seen, the peak value of the averaged Lyα events produced a 0.85% increase in emission with respect to the background, which is higher than the 0.1%–0.3% increase reported by Milligan (2021). The difference may result from the different criteria for event selection, i.e., in our sample, the Lyα events were detected from the Lyα observations itself while the Lyα events in Milligan (2021) were determined from the GOES SXR flare list. The average peak time in Lyα is found to delay by about 20.48 s relative to the SXR peak time, possibly that the Lyα events have a thermal origin on average.

Figure 3(b) shows histogram of the time difference (t_p) between Lyα and corresponding SXR emission peaks. For

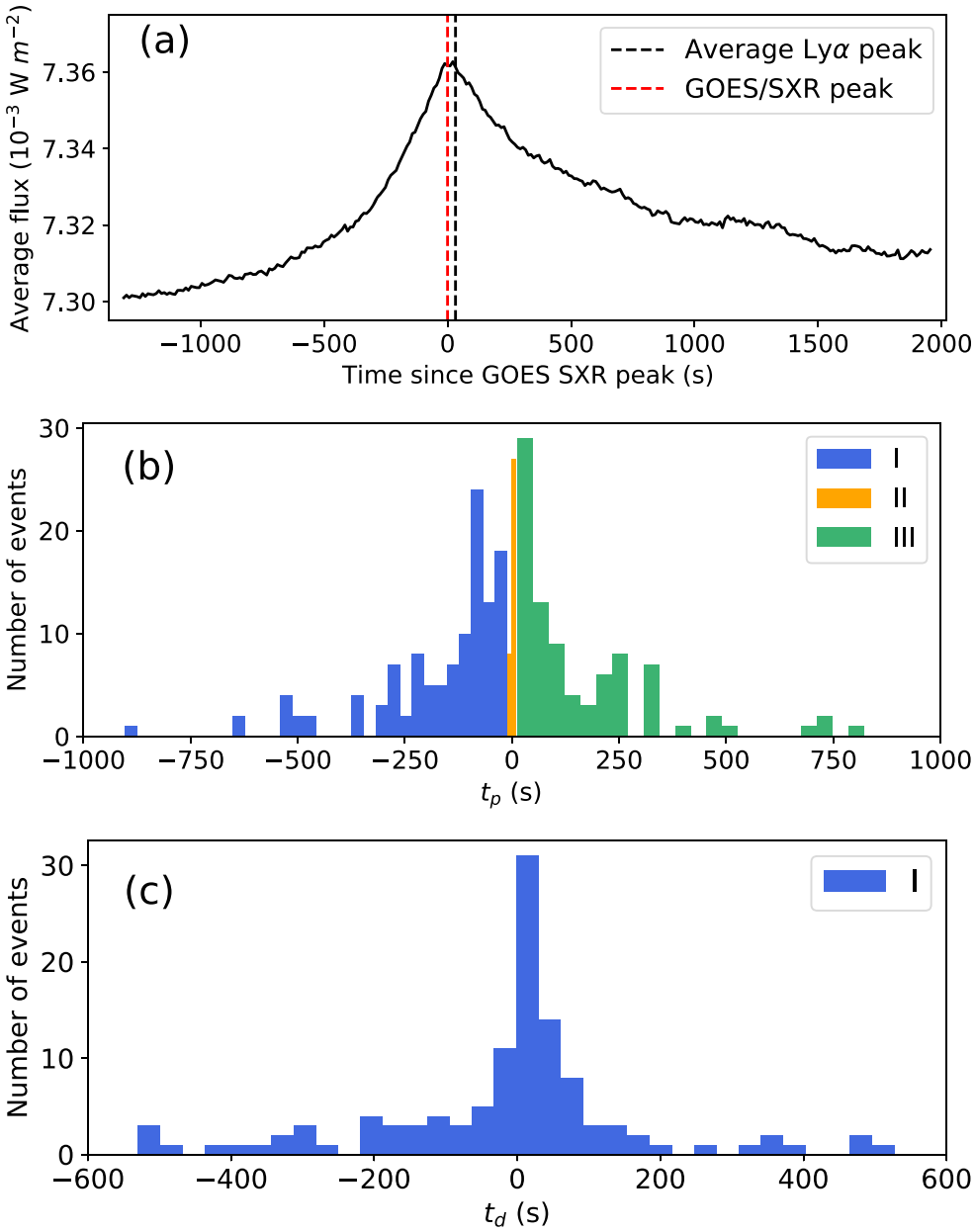

Figure 3. Statistical results of 242 B-class Lyα events. (Top) The average Lyα time profile obtained by aligning to the SXR peak time and averaging them after superposition. The red and black dashed lines mark the SXR peaks and the average peak of the Lyα emission, respectively. (Middle) Histogram of the peak time difference (t_p) between the Lyα and SXR emissions, and (bottom) the histogram of the time difference (t_d) between the Lyα peak and the SXR time-derivative peak. (b), (c) Blue, yellow and green colors represent the results for type I, II, and III B-class flares, respectively.

majority (∼80%) of the B-class flares under study, the peak time of type I events in Lyα is mainly 3 minutes earlier than that of corresponding SXR flares, and the peak time of type III Lyα events is mainly 4 minutes later than that in SXR emission.

To check the Neupert effect (Neupert 1968; Nusinov et al. 2006) in Lyα emission of type I flares, we study the time consistency between the Lyα emission and the time derivative of the corresponding SXR flux. Note that type II and III flares more probably have thermal origin. Therefore, we only investigate the Neupert effect for type I flares in the current paper.

Figure 3(c) shows histogram of the time difference (t_d) between the Lyα peak and the peak of the time derivative of

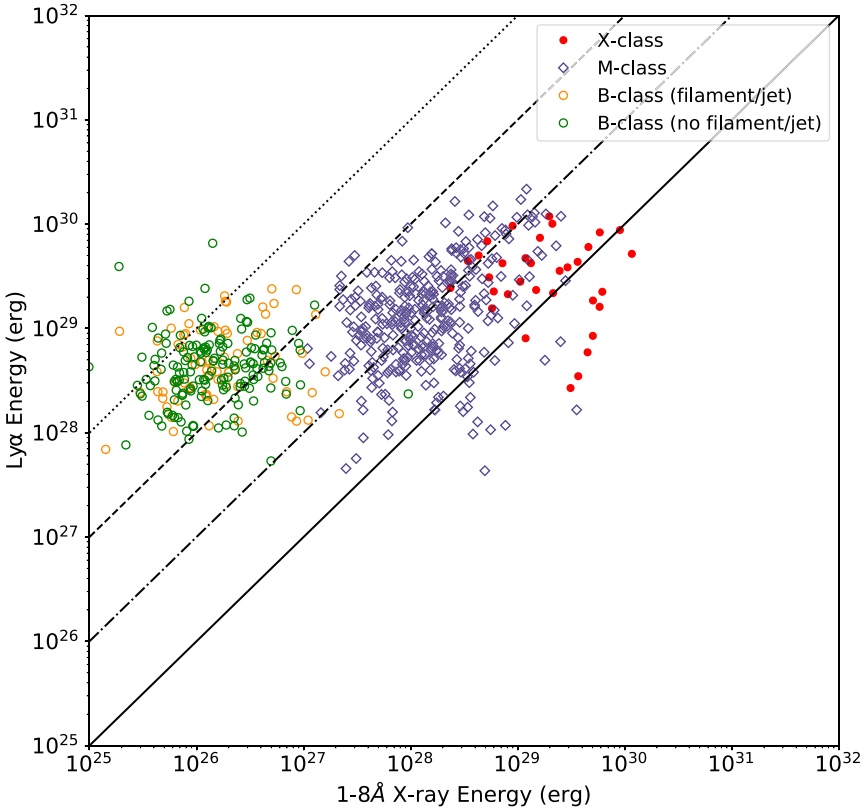

Figure 4. The panel shows scatter plot of Lyα excess radiated energy and total excess radiated energy in GOES 1–8 Å band, which obtained by observation. The lines from top to bottom represent the 1:1, 1:10, 1:100, and 1:1000 ratios, respectively. The yellow and green hollow circles represent B-class flares, which are distinguished by whether they have concurrent filament/jet. The classification principles are detailed in Section 3. The blue diamonds represent M-class flares, and red solid circles represent X-class flares. All the data were calculated with background subtracted.

the SXR flux. We found that for ~80% of type I Lyα flares, t_d falls within $\pm$4 minutes, which is higher than the $\pm$2 minutes difference found for large flares by Jing et al. (2020). This may indicate that a significant number of type I B-class flares follow the Neupert effect, but this effect may not work as well as that in larger flares. However, as we will see below, the consistence with the time derivative of SXR flux may not always indicate a non-thermal origin in the B-class Lyα flares.

4.2. Calculation of Flare Radiation Energy

A solar flare consists of electromagnetic radiations over a broad wavelength range, i.e., from γ-ray through EUV and UV to radio waves, and so far we have no simultaneous observations of some regions of the spectrum. Therefore, determination of the total radiant energy of a solar flare is still a tough work.

The radiant energy of the solar flares in Lyα and SXR was estimated by integrating their time profiles between the start and end times of each flare, and the physical unit W m^{-2} of the solar irradiance/flux measured near Earth (1 au) was converted to erg s^{-1} with 1 W $m^{-2} = 2\pi(1\ \text{au})^2 \times 10^7$ erg $s^{-1} = 1.406 \times 10^{30}$ erg s^{-1} (Milligan et al. 2020).

Before the integral, the background emission was subtracted. We used the greater value of the Lyα event start and end fluxes as background value, consistent with the background subtraction of Lu et al. (2021). We check different background subtraction methods, such as choose a constant fitted with a 24 hr period as the background value (Milligan et al. 2020) and made a background subtraction by averaging the pre-flare flux from one hour before the event onset (Jing et al. 2020). The results show that different background subtraction does not affect our conclusions about the energy distribution of Lyα events in this subsection.

Figure 4 presents the scatter plot of the energy radiated in Lyα versus that in SXR, which shows that the weaker the SXR flare, the more dominant the Lyα emission. For instance, the Lyα radiated energy of X-class flares is around 1–10 times the energy radiated in SXR, while that of M-class flares is around 10–100 times, which is consistent with the results of Milligan et al. (2020). However, for B-class flares, the Lyα radiated energy relative to that in SXR is even higher (100–1000 times

the SXR flare energy). This indicates that even though the GOES class level of the solar flares is very low, the Lyα radiated energy cannot be ignored.

5. Thermal and Non-thermal Properties of Type I Microflares

According the Neupert effect (Neupert 1968), the time derivative of the SXR fluxes is well correlated with the hard X-ray fluxes, which are believed to result from nonthermal electron beams accelerated during solar flares. Below we focus on a few type I events, during which the Lyα emission shows similar temporal evolution to the time derivative of the SXR fluxes. However, as we will see, their thermal and nonthermal properties may differ from one case to another.

5.1. The Flare on 2011 September 7

The flare starting from about 18:24 UT on 2011 September 7 is classified as a B9.1 flare according to the GOES 1–8 Å peak flux around 18:28 UT (red curve in Figure 5(a)). During the flare, the Lyα emission reaches its first peak (P1) at 18:25:14 UT, and its second peak (P2) at 18:26:52 UT (black curve in Figure 5(a)). P2 is much stronger than P1 and was found to closely coincide with the time derivative of the GOES 1–8 Å flux (blue curve in Figure 5(a)). Figure 5(b) presents the RHESSI light curves in 3–6 keV, 6–12 keV, 12–25 keV, and 25–50 keV, respectively, among which the light curves above 12 keV also show impulsive peaks around P1 and P2. This may suggest a nonthermal origin of the Lyα emission.

To confirm this, we then perform spectral analysis of the RHESSI observations during the flare. The spectra ranges from 3 to 40 keV, with a spectral resolution of $1/3$ keV between 3–10 keV and 1 keV between 10–40 keV (Feng et al. 2013). To enhance the flare signal, the spectra were integrated over 20 s. The model we used to fit the spectra consists of a single thermal component (vth) and a nonthermal component (thick2_vnorm).

Figures 6(a)–(c) show the fitting results around P1, P2, and the peak time of SXR emission. As can be seen, the RHESSI X-ray spectra can be well fitted by the combined model of vth +thick2_vnorm, with low-energy cutoffs of 10–18 keV.

It is worth mentioning that the electron fluxes at 50 keV reference energy for the Lyα peak emissions (P1 and P2) were found to be about 1.1×10^{31} s keV^{-1} and 2.4×10^{31} s keV^{-1}, respectively; the spectral index is hard, and the effect of nonthermal fitting is better than that of SXR emission peak time.

Using the combined model, we fitted the RHESSI X-ray spectra through the time interval 18:23–18:30 UT, and the time evolution of the obtained spectral indices as well as the electron flux at 50 kev reference energy are plotted in Figure 5(c). Around the P2 peak times of Lyα emission, the spectral indices of hard X-ray emission became hard and the electron flux significantly increased, indicating that Lyα emission may have a nonthermal component.

In Figure 5(d), we show the fitted time evolution of plasma temperature and nonthermal power, the latter of which was calculated with the routine "calc_nontherm_electron_energy_-flux.pro" in SSWIDL (Saqri et al. 2022). The non thermal power showed a significant increase at the P2 peak of Lyα, while the temperature change was not obvious. These evidences indicate that a large number of nonthermal electrons are produced during the enhancement of Lyα emission.

To show the source region of the nonthermal emission, the RHESSI X-ray images in 3–6 keV, 6–10 keV and 10–25 keV were reconstructed with the "clean" algorithm (e.g., Battaglia et al. 2021), and overlaid on AIA 304 Å images (Figures 6(d)–(f)). As can be seen, during P1 and P2, the nonthermal emission mainly arises from north footpoint of the flare, while at the peak time of SXR emission, the RHESSI sources was slightly merged and moved upward slightly. The evolution of RHESSI sources is consistent with the scenario of chromospheric evaporation, in which the nonthermal electrons bombard the low solar atmosphere, causing the filling of flare loops with hot plasma (García-Alvarez et al. 2005; Milligan & Dennis 2009).

5.2. The Flare on 2010 October 23

The SXR flare on 2010 October 23 started from about 17:31 UT, peaked around 17:38 UT, and then underwent a gradual decay phase, and was classified as a B3.6 flare according to the peak GOES 1–8 Å flux. The corresponding Lyα emission shows a significant peak at about 17:33 UT, which coincides with the time derivative of the GOES SXR fluxes (Figure 7(a)).

In Figure 7(b), we show the corresponding RHESSI light curves in 3–6 keV, 6–12 keV and 12–25 keV, respectively. We found that the light curves below 12 keV show gradual thermal emission as that in GOES 1–8 Å while the light curve in 12–25 keV shows an impulsive but weak peak around the peak time of Lyα emission, possibly implying the production of nonthermal electrons during the flare. To clarify this, we then perform the spectral fitting to the RHESSI spectral observations, as done in Section 5.1.

Figures 8(a)–(c) show the fitting results of the RHESSI spectra observed during the pre-flare phase, around the peak times of the Lyα and SXR emissions, respectively. We found that the pre-flare spectra and the spectra around the Lyα peak can be well fitted with the combined thermal and nonthermal model, while at the peak time of SXR emission, the spectra is better fitted with a double thermal model. Moreover, the electron flux around the Lyα peak was estimated to be 2.1×10^{30} s kev^{-1}, which is much higher than that during the pre-flare phase ($\sim 8.5 \times 10^{27}$ s kev^{-1}). Figures 7(c) and (d) show the temporal evolution of RHESSI fitting parameter and the nonthermal power during 17:30–17:38 UT. As can be seen, the nonthermal power, temperature increase and decrease almost synchronously with the Lyα emission.

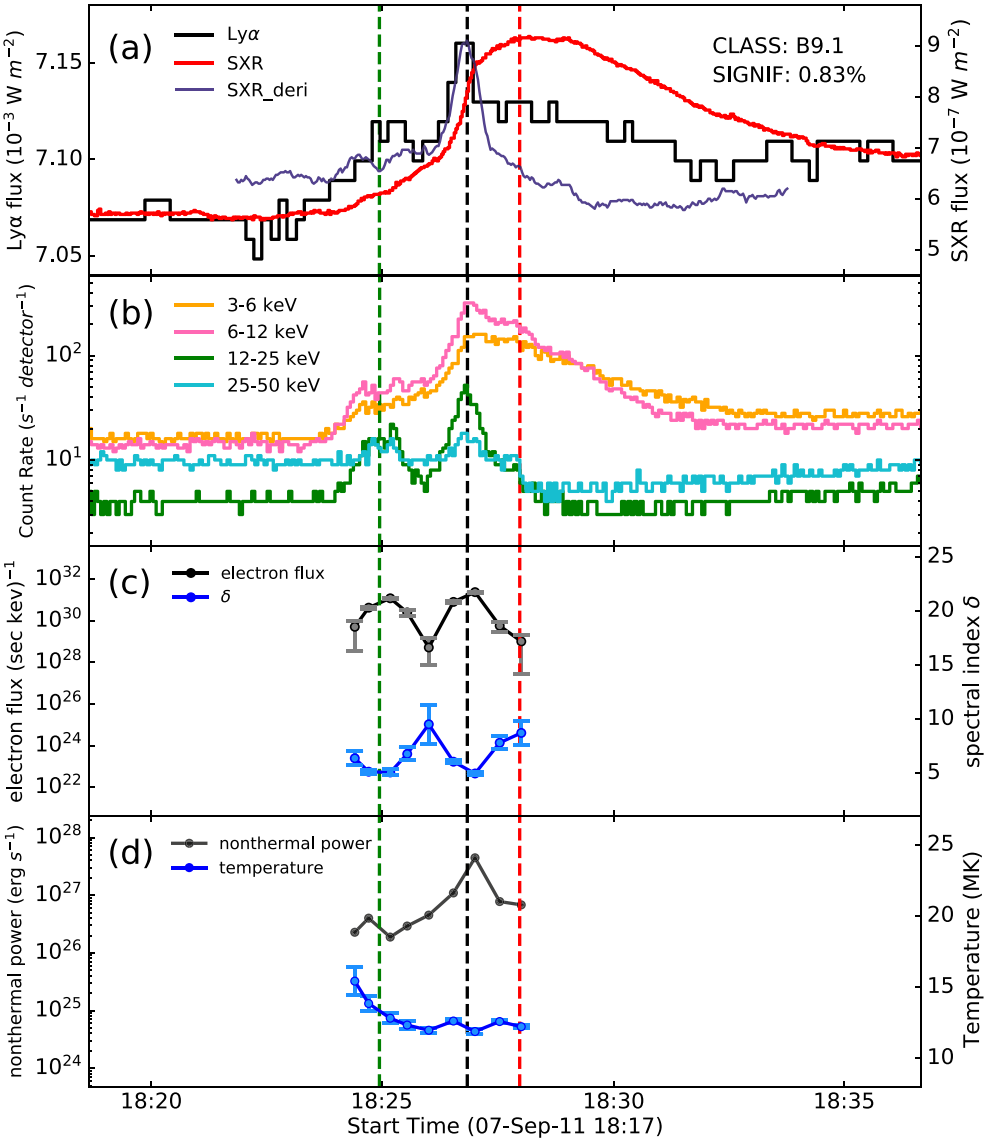

Figure 5. (a), (b) The light curves in Lyα and SXR and the RHESSI count rate in 3–6 keV, 6–12 keV, 12–25 keV and 25–50 keV bands of the flare in Section 5.1. The black and red curves in (a) represent the Lyα and 1–8 Å SXR flux, respectively. (c), (d) The time evolution of the electron flux at 50 keV reference energy, spectral index, temperature and nonthermal power derived from the thick target fit to the spectra at 18:24 UT-18:29 UT, the time interval of each spectral fitting is 20 s. The black and blue curves mark the total integrated electron flux and the spectral index respectively. The green and black vertical dashed lines mark the first peak (P1) and second peak (P2) of Lyα emission, respectively; the red vertical line marks the peak of SXR flux.

These evidences indicate the existence of both nonthermal source and thermal source of Lyα emission.

Figures 8(d)–(f) show the source region of the X-ray emission in 3–8 keV and 8–12 keV, overlaid on concurrent AIA 304 Å images. In the pre-flare phase (Figure 8(d)), there were two X-ray sources in the active region. Around the peak time of Lyα emission (Figure 8(e)), these X-ray sources connected and located at a flare ribbon. Then the 8–12 keV source gradually weakened, this process is consistent with the characteristics of chromospheric evaporation, but is different from the situation in Section 5.1. We notice that the RHESSI map has no source higher than 12 keV. It has less nonthermal emission and the Lyα emission enhancement is more likely to be caused by thermal conduction (Milligan 2008).

5.3. The Flare on 2011 December 18

The flare on 2011 December 18 was classified as a B7.8 flare according to the GOES 1–8 Å peak flux. The time evolution of Lyα emission is highly consistent with the time derivative of

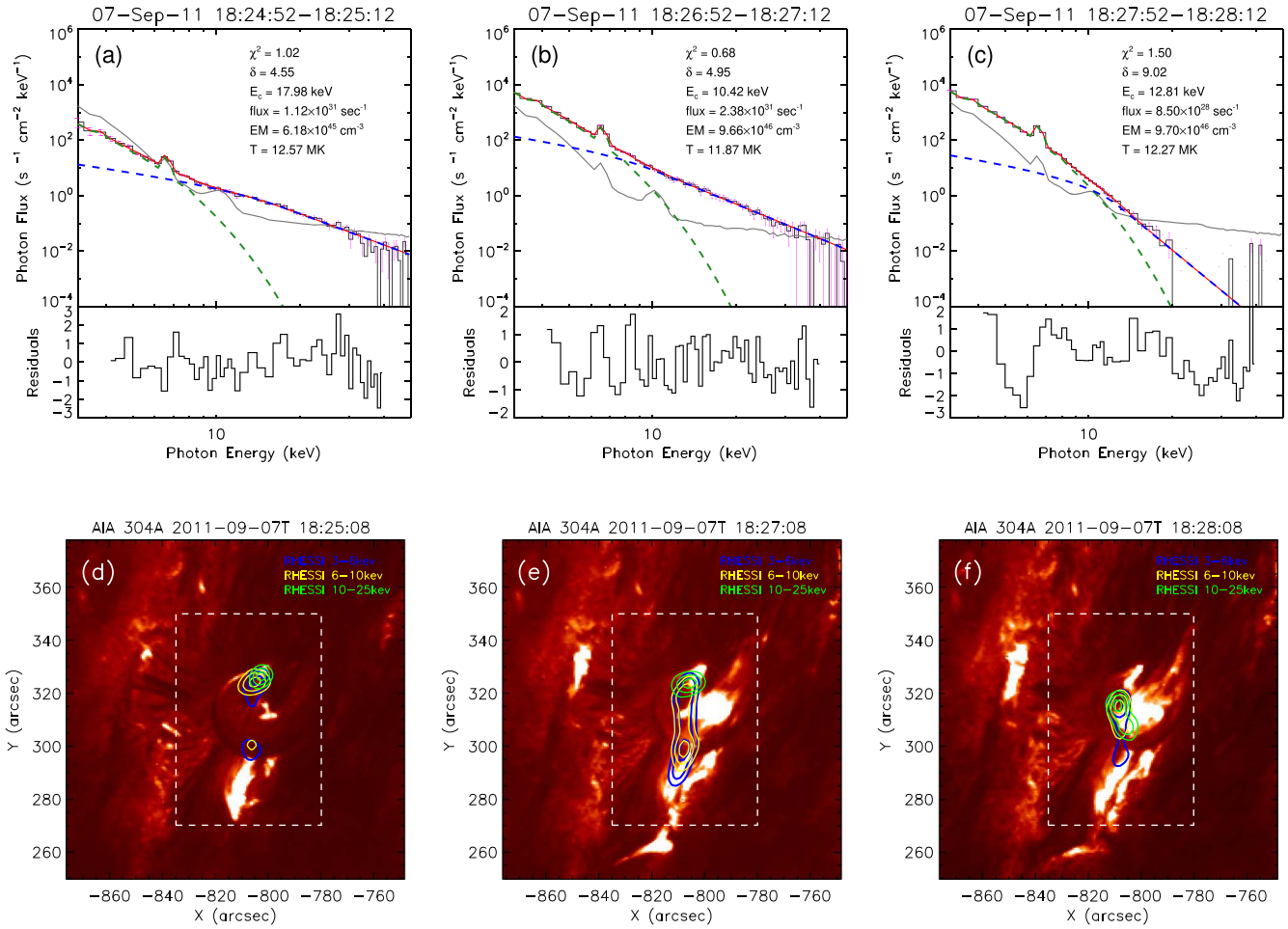

Figure 6. (a)–(c) The RHESSI spectral fitting results in a 20 s interval with the thermal (green) and nonthermal (blue) components around the Lyα peak emissions (P1 and P2) and the peak time of SXR emission for the flare in Section 5.1. The background-subtracted spectral data is shown in black, the red line is the fitting of the combined model of vth+thick2_vnorm. The solid gray line represents the background spectrum. δ represents the spectral index of the non-thermal electron distribution, E_c is the low-energy cutoff of the non-thermal electron, and T and EM are temperature and the total emission measure. The spectral data are all marked with error bars in pink and the normalized residuals are shown at the bottom of the spectra. (d)–(f) Contours of the reconstructed RHESSI clean maps in 3–6 keV (blue), 6–10 keV (yellow) and 10–25 keV (green) bands, and overplotted on the AIA image at 304 Å. The contours are 50%, 70% and 90% levels of maximum emission in each image. The time intervals for the bottom panels from left to right is from 18:24:24 UT to 18:25:54 UT, 18:26:44 UT to 18:27:44 UT and 18:27:44 UT to 18:28:44 UT.

GOES 1–8 Å flux (Figure 9(a)). Figure 9(b) shows corresponding RHESSI light curves in 3–6 keV and 6–12 keV. Note that, RHESSI did not show clear emission enhancement above 12 keV. We found that the RHESSI X-ray emission peaks during the decay phase of Lyα flare, but earlier than the peak time of the SXR emission.

In order to clarify the origin of the Lyα and X-ray emission, we perform the spectral analysis of the RHESSI X-ray emission, as done previously. We found that RHESSI spectra are better fitted with a single thermal component (vth). The fitting results around the peak times of the Lyα, RHESSI and SXR emission are shown Figures 10(a)–(c), respectively. Figure 9(c) shows the temporal evolution of the obtained plasma temperature during the whole flare. We found that the plasma temperature increases synchronously with the Lyα emission, and reaches a peak value of about 10.23 MK around the peak time of Lyα emission. This result is consistent with the characteristics of the chromospheric evaporation caused by thermal conduction (Milligan 2008).

5.4. The Event on 2012 March 29

The event on 2012 March 29 started from about 23:17 UT, peaked at 23:24 UT, and was classified as a B6.2 flare according to the GOES 1–8 Å flux. The Lyα emission peaks about 5 minutes earlier than the SXR peak (Figure 1(c)). Different from the above-discussed flares, the Lyα curve of this

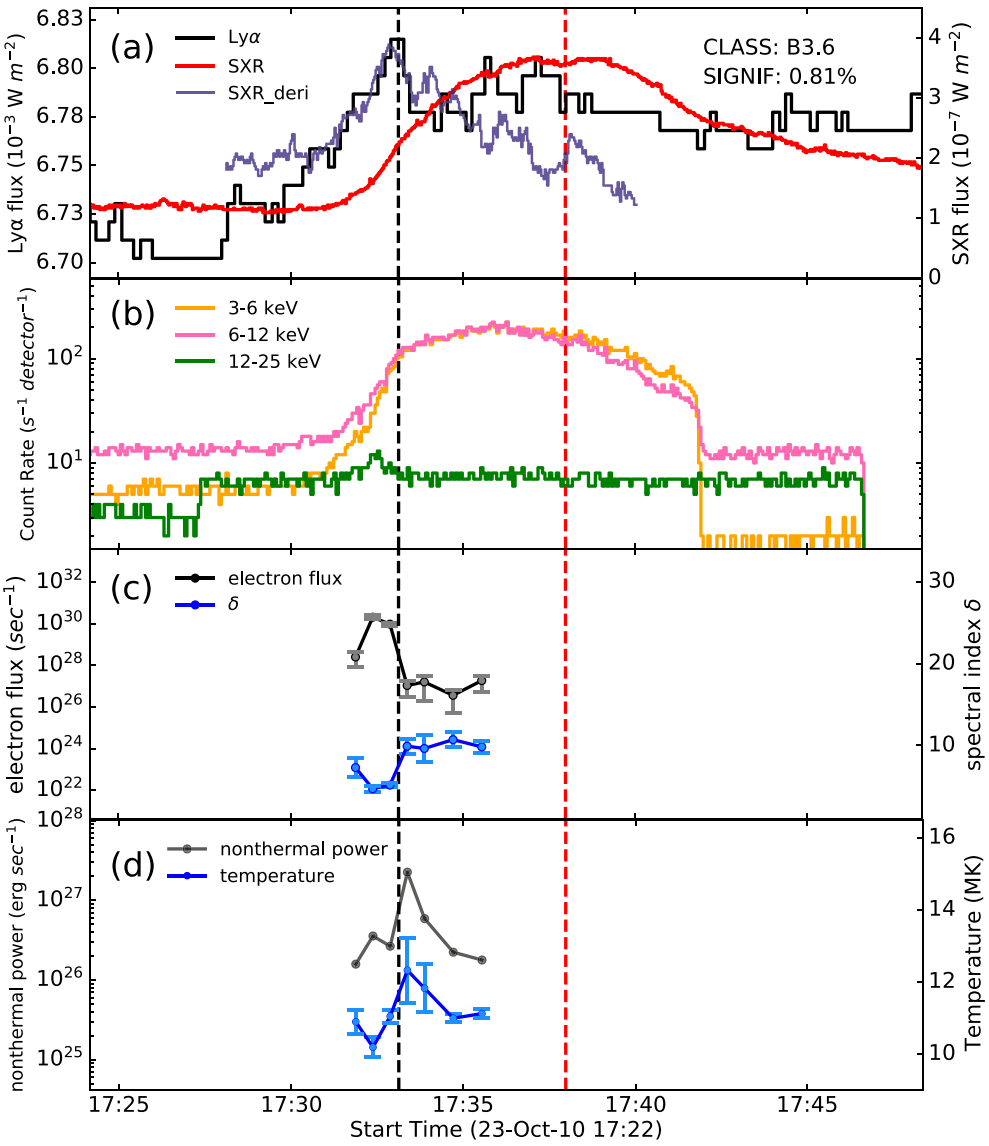

Figure 7. (a), (b) The light curves in Lyα and SXR and the RHESSI count rate in 3–6 keV, 6–12 keV, 12–25 keV bands of the flare in Section 5.2. (c), (d) The time evolution of the electron flux at 50 keV reference energy, spectral index, temperature and nonthermal power derived from the thick target fit to the spectra at 17:30 UT–17:37 UT, the time interval of each spectral fitting is 20 s. The black and red vertical dashed lines mark the peak of Lyα and SXR emissions, respectively. All the other curves and lines have the same meanings as the ones in Figure 5.

event does not coincide with the time derivative of the SXR flux, which means that the Lyα emission may have no relationship with the flare. To confirm this, we checked AIA images in 304 Å (Figures 11(a)–(c)). Before the flare (at about 23:13 UT), an active region filament already existed. In five minutes at about 23:18 UT, the filament erupted, accompanied by a strong increase of Lyα emission. Then at about 23:23 UT, flare loops were observed.

This event indicates that the Lyα emission enhancement originates not only from the solar flare, but also from the erupted filament. The Lyα emission from filaments can not only occur in the decay phase of the flare (Wauters et al. 2022), but also in the preflare phase. In this event, the filament eruption may lead to the initiation of the flare.

5.5. Energy Calculations and Discussions on Thermal and Nonthermal Properties

In Sections 5.1, 5.2 and 5.3, we present some important properties of three typical type I Lyα flares, and Section 5.4 presents a special case that is related with an erupted filament.

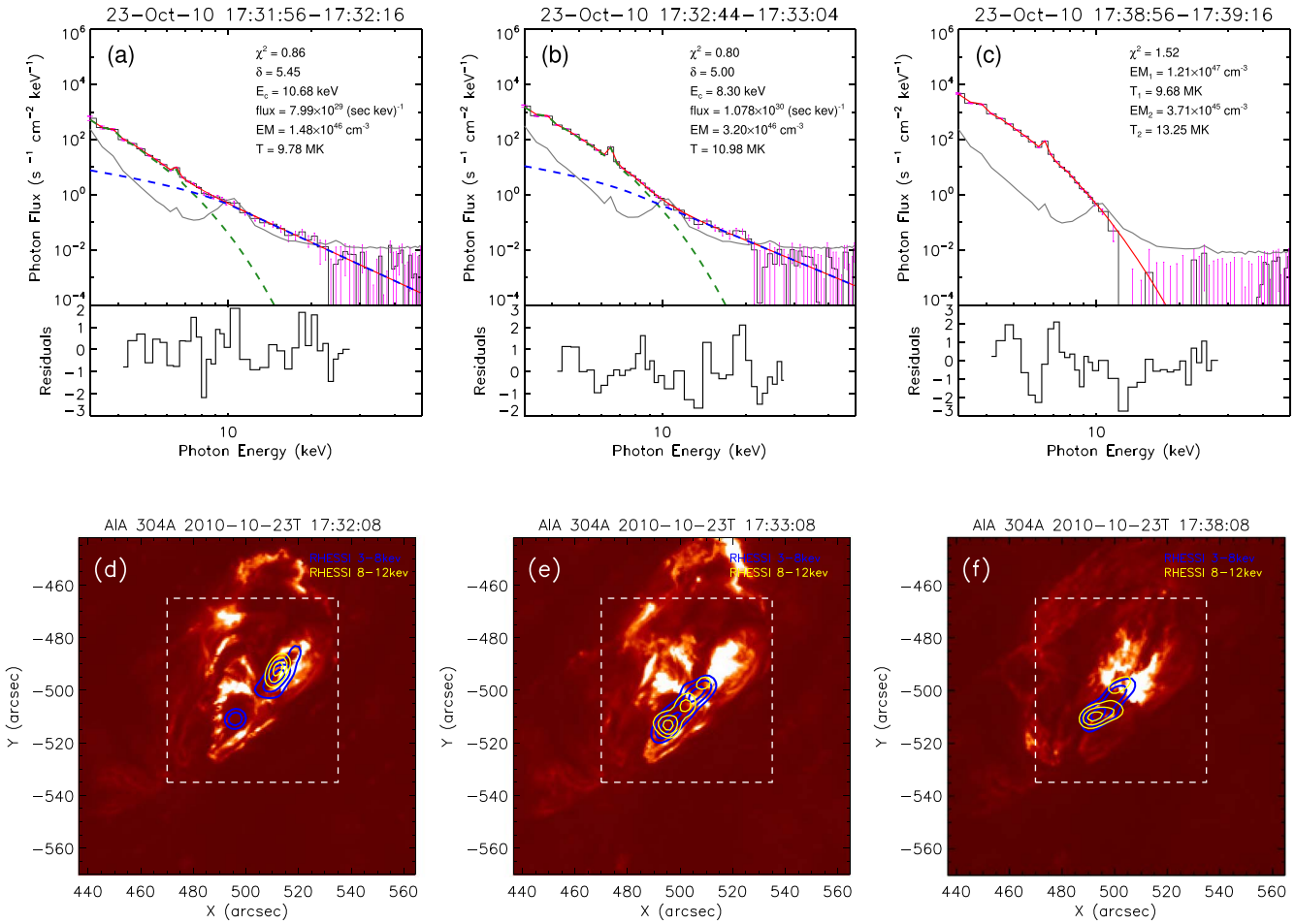

Figure 8. (a)–(c) The RHESSI spectral fitting results in a 20 s interval during the pre-flare phase, around the peak times of the Lyα and SXR emissions for the flare in Section 5.2. The spectra of (a) and (b) were fitted with the thermal (green) and nonthermal (blue) components, while the spectra of (c) were fitted with a double-thermal component (red). Other lines and fitting parameters of the top panels have the same meanings as the ones in Figure 6. (d)–(f) Contours of the reconstructed RHESSI clean maps in 3–8 keV (blue), 8–12 keV (yellow) bands, and overplotted on the AIA image at 304 Å. The contours are 50%, 70% and 90% levels of maximum emission in each image. The time intervals for the bottom panels from left to right are from 17:31:08 UT to 17:32:38 UT, 17:32:48 UT to 17:34:18 UT and 17:37:48 UT to 17:39:18 UT.

Here we give some discussions about them. For convenience, the flares presented in Sections 5.1, 5.2 and 5.3 will be referred as SOL2011-9-7, SOL2010-10-23 and SOL2011-12-18, respectively.

To separate thermal and nonthermal emissions during these flares, we performed the RHESSI spectra analysis. The spectra of flares SOL2011-9-7 and SOL2010-10-23 can be well fitted with a combined thermal and nonthermal model, while the spectra of SOL2011-12-18 is better fitted with only the thermal component. Based on the fitting results, the thermal and nonthermal energies can be estimated.

The thermal energy ($E_{\rm th}$) of the flares was calculated via the following formula (Emslie et al. 2012; Feng et al. 2013; Aschwanden et al. 2015):

$$E_{\rm th} = 3n_e k_B T f V = 3k_B T\sqrt{\rm EM \times fV}, \quad (1)$$

where n_e is the electron density, k_B is the Boltzmann constant, T is the plasma temperature, EM is the total emission measure, V is the volume of the flare loop in SXR, and f is the volumetric filling factor.

In this paper, EM and T were obtained by fitting the RHESSI X-ray spectra with a specific model, and the volume was estimated via $V = A^{3/2}$, where A is the area of thermal emission that was estimated by the pixels within the 50% contour of RHESSI 3–8 keV images (For these flare events, 3–8 keV is below their low energy cutoff and it can be considered that electrons in this energy range are thermal). (Emslie et al. 2004; Feng et al. 2013).

According to Equation (1) and assuming a filling factor of 1 (Veronig et al. 2005), the thermal energies of SOL2011-9-7, SOL2010-10-23 and SOL2011-12-18 are estimated to be 3.83×10^{29} erg, 3.03×10^{29} erg, and 5.09×10^{29} erg, respectively. The

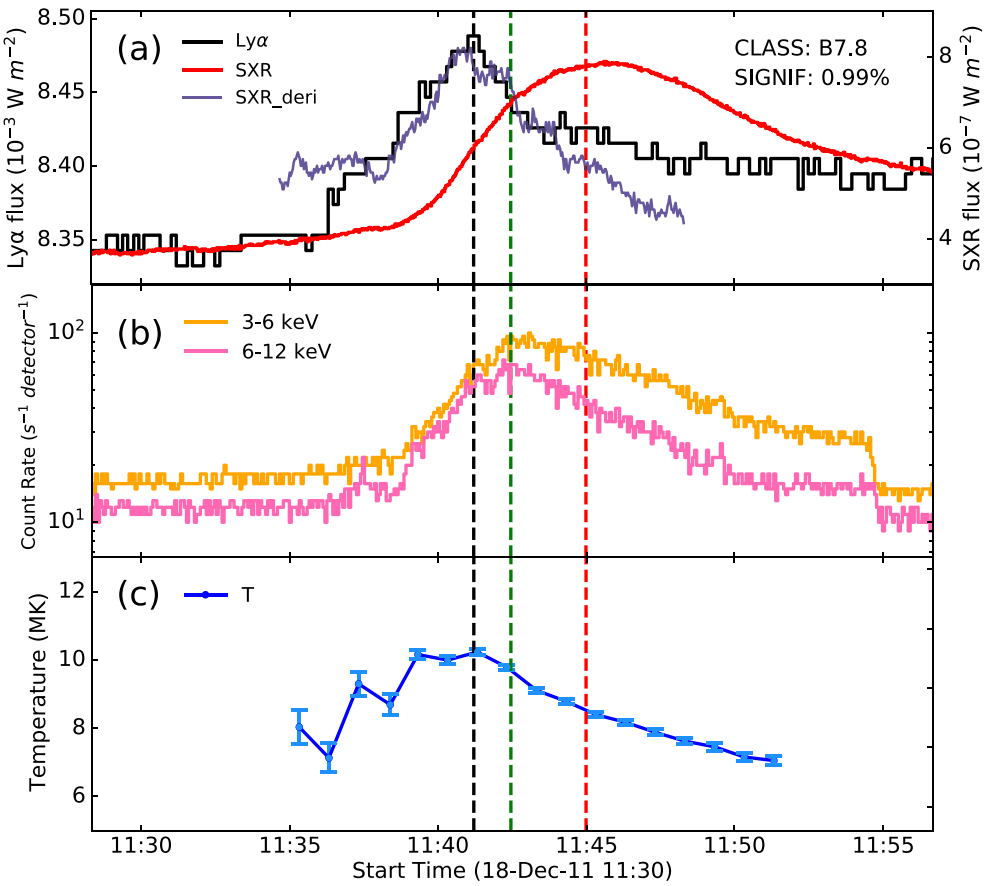

Figure 9. (a), (b) The light curves in Lyα and SXR and the RHESSI count rate in 3–6 keV, 6–12 keV bands of the flare in Section 5.3. (c) The time evolution of the plasma temperature derived from the single thermal fit to the spectra at 11:35 UT-11:51 UT, the time interval of each spectral fitting is 20 s. The blue curve represents the plasma temperature. The black and red vertical dashed lines mark the peak time of Lyα and SXR emission respectively, the green vertical line marks the peak time of RHESSI curves in 3–12 keV. All the other curves and lines have the same meanings as the ones in Figure 5.

nonthermal energy is calculated with the nonthermal power (Saqri et al. 2022) and integrated over the flare time (Emslie et al. 2004). According to the calculation, the nonthermal energies of SOL2011-9-7 are 1.48×10^{29} erg, higher than that of SOL2010-10-23.

Here we use the nonthermal power and the nonthermal electron beam area to estimate the electron beam flux at the peak of Lyα emission. The electron beam area is determined by the area within the 50% contour of the RHESSI images above the low energy cutoff. Comparing to flare SOL2011-9-7, the electron beam flux and the nonthermal plasma energy of SOL2010-10-23 are lower.

In addition, we briefly compared the nonthermal energy to the Lyα radiated energy of the three events to better understand whether the nonthermal energy is sufficient to power the Lyα losses.

For the SOL2011-9-7 flare, the Lyα radiated energy was 3.24×10^{28} erg, and the nonthermal energy was 1.48×10^{29} erg, which is sufficient to drive the Lyα radiation. However, the nonthermal energy of SOL2010-10-23 is 8.06×10^{28} erg, slightly lower than its Lyα radiation energy (1.79×10^{29} erg), which means that the Lyα emission need to rely on both thermal and non-thermal drive.

These calculations all show that the Lyα emission of SOL2010-10-23 and SOL2011-9-7 both had contributions from nonthermal electrons, while the non-thermal component of the former was more significant.

As for SOL2011-12-18, it may not contain nonthermal emission and there is no obvious movement trend of the source from the RHESSI image (it may be that the timescale of thermal conduction is too short), we believe that it is probably driven by thermal conduction.

In conclusion, although all light curves of the three Lyα flares under study have their Lyα peak consistent with the SXR time-derivative peak, their non-thermal and thermal properties are different. The SXR time derivative of SOL2011-9-7 and SOL2010-10-23 corresponds to the injection of nonthermal electrons, although SOL2010-10-23 has less nonthermal

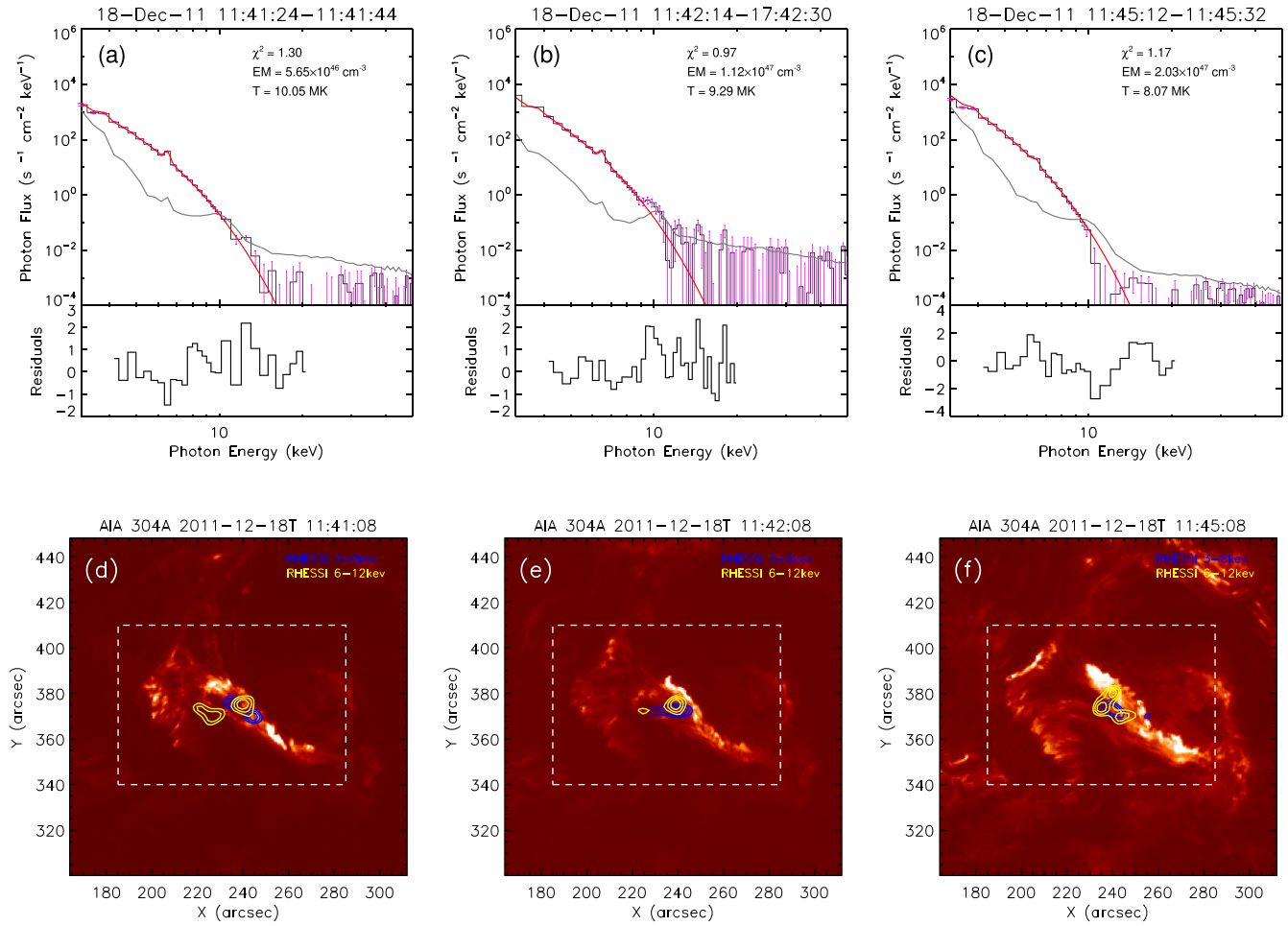

Figure 10. (a)–(c) The RHESSI spectral fitting results in a 20 s interval around the peak times of the Lyα, RHESSI and SXR emission for the flare in Section 5.3. The spectrum of (a)–(c) was fitted with a single thermal (red) component. All the lines and fitting parameters of the top panels have the same meanings as the ones in Figure 6. (d)–(f) Contours of the reconstructed RHESSI clean maps in 3–6 keV (blue) and 6–12 keV (yellow) bands, and overplotted on the AIA image at 304 Å. The contours are 70%, 80% and 90% levels of maximum emission in each image. The time intervals for the bottom panels from left to right are from 11:40:26 UT to 11:41:56 UT, 11:41:56 UT to 11:43:26 UT and 11:44:56 UT to 11:46:26 UT.

energy. while the SXR time-derivative peak of SOL2011-12-18 is more probably caused by thermal conduction. These results reveal that the coincidence of the Lyα peak with the SXR time-derivative peak is not a sufficient condition of the nonthermal property of a Lyα flare.

We summarize all the above calculation results in Table 2, to better analyze and compare the differences between the thermal and non-thermal properties of the three flares.

6. Interpretations of the Delay of Lyα Peaks For Type III Events

In our event list, the number of type III events with Lyα peak later than SXR peak accounts for about 36.78% of the total, which is larger than the statistical result of M- and X-class flares (type III flares account for ∼21.7% of the total) (Jing et al. 2020). Below we examine two cases. In one case, the delayed Lyα emission results from the erupted filament and in the other case, the delayed Lyα emission is due to the successive cooling of the hot flare loops.

6.1. The Event on 2015 February 14

Figure 12(a) shows the light curves of Lyα and SXR emissions on 2015 February 14. The SXR flare peaked at 12:44 UT and was classified as B7.1. Then a few minutes later (12:51 UT), the Lyα emission reaches its peak value. Figure 12(b) shows the temporal evolution of the integrated EUV emission from AIA images over the subregion (dashed box) shown in Figures 12(c) ∼ (f), which show a filament eruption. We note that the 304 Å light curve shows a similar trend as the Lyα curve in the rise phase of the event (12:25 UT ∼ 12:44 UT), but

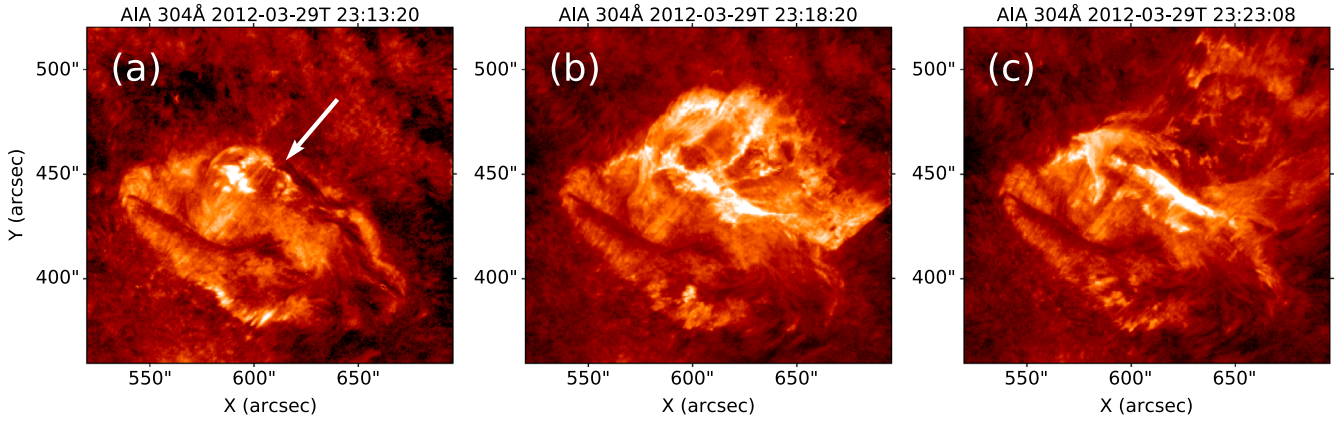

Figure 11. The SDO/AIA 304 Å images of the type I B-class event that occurred on 2012 March 29. The images from left to right occurred before the filament burst, at the peak of Lyα and at the peak of SXR, respectively. The whole process shows the eruption of the filament (a), (b) and the generation of the flare ribbon (c). The white arrow on the left panel indicates the filament. Figure 1(c) shows the light curves of the Lyα and SXR emissions for this event.

Table 2
A Table Summarizing All the Parameters Calculated in Section 5.5 for the Flares SOL2011-9-7, SOL2010-10-23 and SOL2011-12-18

Flare Event	SOL2011-9-7	SOL2010-10-23	SOL2011-12-18
GOES level	B9.1	B3.6	B7.8
The significance index (%)	0.83	0.81	0.99
Estimated volume (cm^3)	2.57×10^{27}	2.69×10^{27}	2.4×10^{27}
Thermal energy (erg)	3.83×10^{29}	3.03×10^{29}	5.09×10^{29}
Nonthermal energy (erg)	1.48×10^{29}	8.06×10^{28}	...
Lyα radiated energy (erg)	3.24×10^{28}	1.79×10^{29}	7.68×10^{28}
SXR radiated energy (erg)	1.58×10^{26}	1.91×10^{26}	2.98×10^{26}
Electron beam flux (erg cm^{-2} s^{-1})	7.05×10^{9}	2.77×10^{9}	...

gradually decreases as the Lyα emission to a secondary peak (around 12:51 UT).

In some EUV wave bands (171 Å, 193 Å, 211 Å and 335 Å), the emission keeps increasing and exhibits a secondary peak around the Lyα peak time. In this event, we do not observe the phenomenon of gradual cooling from the high-temperature to low-temperature wave bands. These indicate that in B-class flares, when the filament was partially heated, there was still sufficient neutral hydrogen to scatter the Lyα radiation from the chromosphere, which produced a delayed enhancement of Lyα emission (Rubio da Costa et al. 2009; Milligan 2021).

6.2. The Flare on 2016 April 15

Similar to the analysis in Section 6.1, we perform studies of the flare on 2016 April 15 (Figure 13), which was classified as a B7.7 flare according to the GOES 1–8 Å peak flux at about 06:26 UT. The Lyα emission peaks about 4 minutes later (around 06:30 UT).The flare loops can be clearly seem from AIA images (Figures 13(c)–(e))).

Figure 13(b) shows time evolution of the integrated emission from the flare active region (dashed box in Figures 13(c)–(e)), which shows that the EUV emissions peaks successively from high- to low-temperature wavelength channels, indicating a cooling process of the hot plasma. The Lyα emission peaks when the plasma cools to a certain temperature range in which the Lyα emission is largely produced (Koza et al. 2019; Jing et al. 2020).

7. Conclusions and Outlook

We established a catalog of Lyα enhancement events associated with SXR flares from 2010 April 8 to 2016 June 6, of which 242, 1428, 365, 33 flares are categorized as B, C, M, and X classes, respectively. We focused on the 242 small B-class flares which are less investigated, however, show non-negligible Lyα emission enhancement. Statistical and detailed case studies are presented to reveal their time properties, energetics, and thermal and non-thermal properties.

The occurrence of B-class flares does not seem to correlate with the total number of sunspots in each year, which is different from the statistical results for M- and X-class flares (Jing et al. 2020). The duration of B-class flares is on average 18 minutes, shorter than that of large M- and X-class flares (~25 minutes). We divided 242 B-class flares with the Lyα emission enhancement into three types, and obtained 118 type I

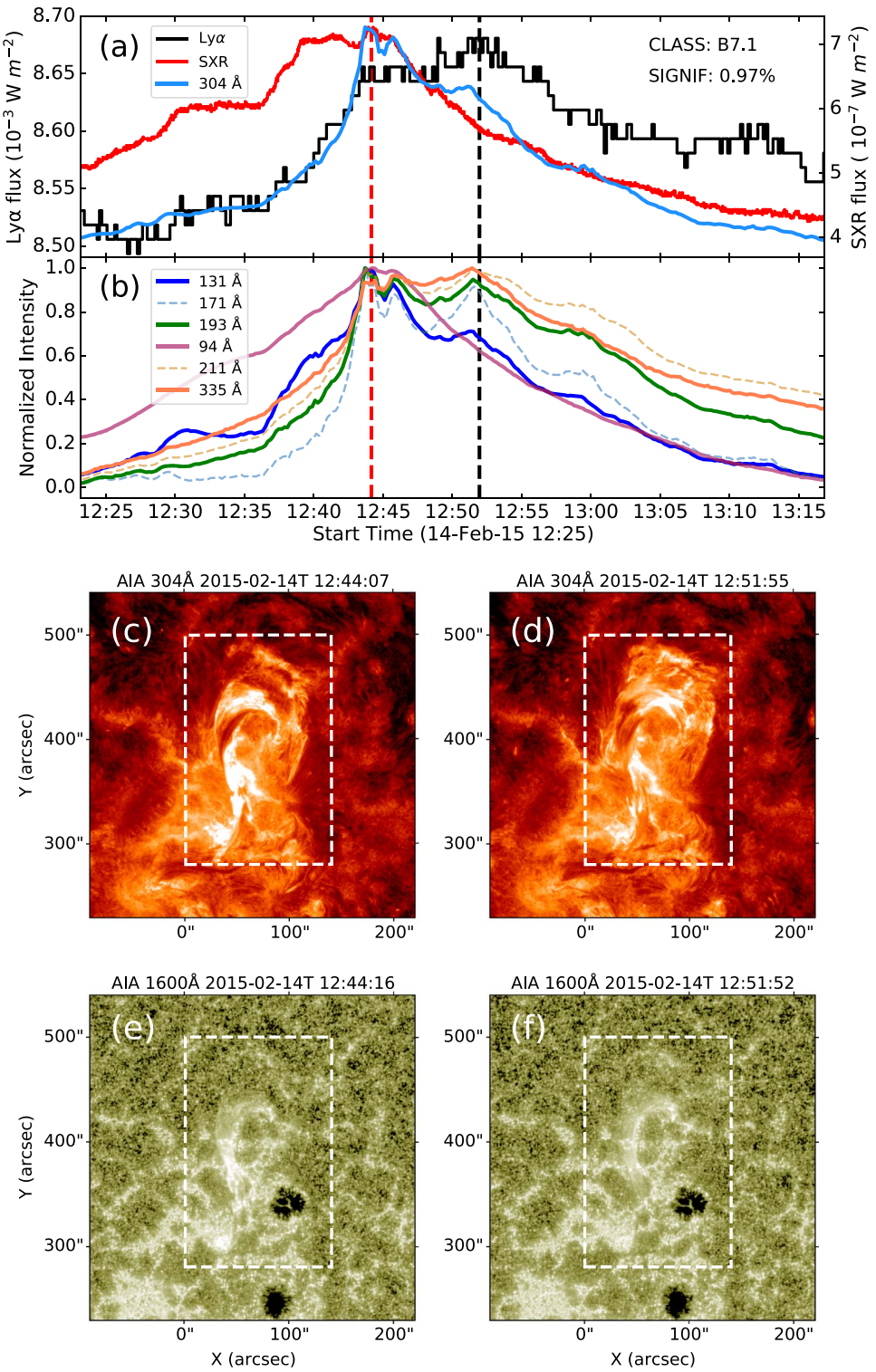

Figure 12. (a) The light curves of SXR, Lyα and 304 Å on 2015 February 14. (b) Normalized curves of integrated flux of AIA pixel values in the white dotted box region in 94 Å (pink), 131 Å (blue), 193 Å (green), 171 Å (light blue), 211 Å (light orange) and 335 Å (orange) wave bands. (c)–(f) The SDO/AIA images at the SXR and Lyα peak of light curves in 304 Å and 1600 Å, respectively. (e), (f) The SDO/AIA images at the SXR and Lyα peak of light curves in 1600 Å respectively. The vertical dashed lines in different colors in the bottom panel represent the peaks of curves in different wave bands. The other curves and lines have the same meanings as the ones in Figure 11(d).

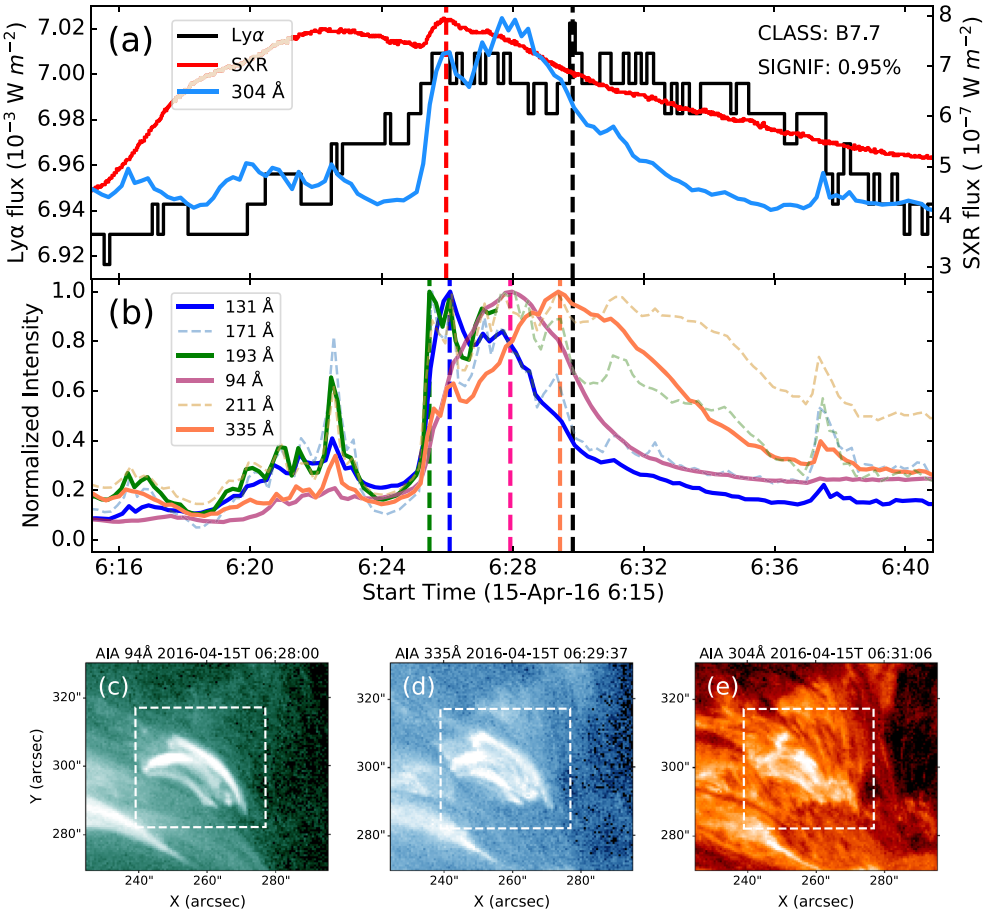

Figure 13. (a) The light curves of SXR, Lyα and 304 Å on 2016 April 15. (b) Normalized curves of integrated flux of AIA pixel values in the white dotted box region in 94 Å (pink), 131 Å (blue), 193 Å (green), 171 Å (light blue), 211 Å (light orange) and 335 Å (orange) wave bands. (c)–(e) The SDO/AIA images at the peak time of light curves in 304 Å, 94 Å and 335 Å bands respectively. The vertical dashed lines in different colors in the bottom panels represent the peaks of the curves in different wave bands. The other curves and lines have the same meanings as the ones in Figure 11(d).

events, 35 type II events and 89 type III events. Compared with the results of large flares by Jing et al. (2020), the proportion of type I events decreases and the proportion of type II/III events increases, suggesting B-class Lyα events may have more thermal emission than large flares.

By aligning and averaging the time profile of these Lyα emission enhancement events, we found that the average Lyα peak is 0.85% stronger than the background, and the average Lyα peak is only 20.48 s later than the SXR peak. The enhancement is slightly higher than 0.1%–0.3% obtained by Milligan (2021). In the aspect of the time difference between the Lyα and SXR emission peak, 80% of the type I and III events have a time difference less than 220 s and 250 s, respectively. To investigate the Neupert effect for type I events, we also checked the time difference of the Lyα peak and the SXR time-derivative peak, and found that it differs by $\pm$240 s. 80% of the events have a difference less than 240 s.

The delay of the Lyα peak in type III Lyα events can be attributed to either the Lyα emission from an erupting filament or cooling of the hot plasma in flare loops to the Lyα channel. We present in the paper two events which illustrate these two interpretations, respectively. In the former case, a filament which experienced a failed eruption, produced a delayed Lyα emission by the neutral hydrogen in it. In the latter case, the peak of EUV light curves gradually evolved from high to low temperatures. The Lyα peak may come from the successive cooling of the thermal plasma in flare loops. On the other hand, interestingly in a type I event, the Lyα peak was even earlier than that of the time derivative of the SXR flux. Its Lyα emission was originated from an erupted filament which may initiate the flare occurrence. Therefore the Lyα emission from filament can occur not only in the decay phase of the flare, but also in the pre-flare phase. Although in some events the Lyα peak corresponds to the filament emission, the Lyα emission from the flare in the same event is still significant.

Concerning the flare energetics, we calculated the energy radiated in Lyα versus that in SXR for all events in this study. For B-class flares, the ratio of the radiated energy in Lyα to that in SXR of about 100–1000 is even higher than that of M- and X-class flares. This indicates that the weaker the SXR flare, the more dominant the Lyα emission.

To investigate the thermal and non-thermal properties and Neupert effect of the B-class flares, we selected three representative type I Lyα flares. The RHESSI spectra and images reveal that the Lyα peak of both SOL2011-9-7 and SOL2010-10-23 flares probably have a nonthermal origin. The nonthermal emission of SOL2010-10-23 was lower, and gradually evolved from nonthermal to thermal. The RHESSI clean maps with time show that the RHESSI sources merged and moved upwards slightly. It is consistent with the scenario of chromospheric evaporation, in which the nonthermal electrons and/or heat conduction increase the pressure in the chromosphere, causing the filling of flare loops with hot plasma. The RHESSI spectra of the SOL2011-12-18 flare and the consistency between the Lyα light curve and temperature evolution indicate that it is more likely a thermal flare.

These three representative events implies that the coincidence of the Lyα peak with the SXR time-derivative peak is not a sufficient condition of the nonthermal origin of a Lyα flare. The Lyα emission enhancement has two possible sources, i.e., nonthermal electrons and thermal conduction. For flares SOL2011-9-7 and SOL2010-10-23, the nonthermal electron beams have a significant contribution to the Lyα emission, while during SOL2011-12-18, it is mainly driven by thermal conduction.

The current statistical work is based on the Lyα light curve of B-class flares integrated over the solar disk. Therefore, we do not have the Lyα images to locate their source regions. Our research suggests that the enhancement of the Lyα emission may be contributed by both microflares and eruptive filaments, but further research will require more Lyα observations.

We plan to extend our analysis on microflares to the Lyα observations by Extreme Ultraviolet Imager (EUI, Rochus et al. 2020) on board Solar Orbiter, and look forward to the full-disk Lyα images provided by the Lyα Solar Telescope (LST, Feng et al. 2019; Li et al. 2019), on board the Advanced Space-based Solar Observatory (ASO-S, Gan et al. 2019, 2022), which was launched in October 2022. It can further verify the thermal and nonthermal properties and the radiation mechanism of Lyα enhancement events.

Acknowledgments

We thank the referee very much for providing detailed suggestions/comments that help us to improve the manuscript. The authors wish to thank NOAA's open data policy for providing targeted data from the instrument website. The data are courtesy of the teams of SDO, RHESSI and GOES. SDO is a mission of NASA's Living With a Star Program. This work is supported by the National Key R&D Program of China under grants 2022YFF0503003 (2022YFF0503000) and 2018YFA0404200, the National Natural Science Foundation of China (NSFC, Grant Nos. 11921003, 11973012, and 11820101002), CAS Strategic Pioneer Program on Space Science (Grant Nos. XDA15018300, XDA15052200, XDA15320103, and XDA15320301), the mobility program (M-0068) of the Sino-German Science Center.

ORCID iDs

Zheng-Yuan Tian https://orcid.org/0000-0002-2158-0249
Hui Li https://orcid.org/0000-0003-1078-3021
Yue Zhou https://orcid.org/0000-0002-3341-0845

References

Aschwanden, M. J., Boerner, P., Ryan, D., et al. 2015, ApJ, 802, 53
Battaglia, M., Sharma, R., Luo, Y., et al. 2021, ApJ, 922, 134
Chamberlin, P. C., Woods, T. N., Didkovsky, L., et al. 2018, SpWea, 16, 1470
Curdt, W., Brekke, P., Feldman, U., et al. 2001, A&A, 375, 591
Dominique, M., Zhukov, A. N., Heinzel, P., et al. 2018, ApJL, 867, L24
Emslie, A. G., Dennis, B. R., Shih, A. Y., et al. 2012, ApJ, 759, 71
Emslie, A. G., Kucharek, H., Dennis, B. R., et al. 2004, JGRA, 109, A10104
Feng, L., Li, H., Chen, B., et al. 2019, RAA, 19, 162
Feng, L., Wiegelmann, T., Su, Y., et al. 2013, ApJ, 765, 37
Gan, W. Q., Feng, L., & Su, Y. 2022, NatAs, 6, 165
Gan, W.-Q., Zhu, C., Deng, Y.-Y., et al. 2019, RAA, 19, 156
García-Alvarez, D., Johns-Krull, C. M., Doyle, J. G., et al. 2005, A&A, 444, 593
Glesener, L., Krucker, S., Duncan, J., et al. 2020, ApJL, 891, L34
Hannah, I. G., Hudson, H. S., Battaglia, M., et al. 2011, SSRv, 159, 263
Hannah, I. G., Krucker, S., Hudson, H. S., Christe, S., & Lin, R. P. 2008, A&A, 481, L45
Hanser, F. A., & Sellers, F. B. 1996, Proc. SPIE, 2812, 344
Hurford, G. J., Schmahl, E. J., Schwartz, R. A., et al. 2002, SoPh, 210, 61
Jing, Z., Pan, W., Yang, Y., et al. 2020, ApJ, 904, 41
Koza, J., Kuridze, D., Heinzel, P., et al. 2019, ApJ, 885, 154
Lemen, J. R., Title, A. M., Akin, D. J., et al. 2012, SoPh, 275, 17
Li, H., Chen, B., Feng, L., et al. 2019, RAA, 19, 158
Li, Z., Su, Y., Veronig, A. M., et al. 2022, ApJ, 930, 147
Lin, R. P., Dennis, B. R., Hurford, G. J., et al. 2002, SoPh, 210, 3
Lu, L., Feng, L., Li, D., et al. 2021, ApJS, 253, 29
Milligan, R. O. 2008, ApJL, 680, L157
Milligan, R. O. 2021, SoPh, 296, 51
Milligan, R. O., & Chamberlin, P. C. 2016, A&A, 587, A123
Milligan, R. O., Chamberlin, P. C., Hudson, H. S., et al. 2012, ApJL, 748, L14
Milligan, R. O., & Dennis, B. R. 2009, ApJ, 699, 968
Milligan, R. O., Hudson, H. S., Chamberlin, P. C., Hannah, I. G., & Hayes, L. A. 2020, SpWea, 18, e02331
Neupert, W. M. 1968, ApJL, 153, L59
Nusinov, A. A., Kazachevskaya, T. V., Kuznetsov, S. N., Myagkova, I. N., & Yushkov, B. Y. 2006, SoSyR, 40, 282
Rochus, P., Auchère, F., Berghmans, D., et al. 2020, A&A, 642, A8
Rubio da Costa, F., Fletcher, L., Labrosse, N., & Zuccarello, F. 2009, A&A, 507, 1005
Saqri, J., Veronig, A. M., Warmuth, A., et al. 2022, A&A, 659, A52
Veronig, A. M., Brown, J. C., Dennis, B. R., et al. 2005, ApJ, 621, 482
Viereck, R., Hanser, F., Wise, J., et al. 2007, Proc. SPIE, 6689, 66890K
Wauters, L., Dominique, M., Dammasch, I. E., et al. 2022, SoPh, 297, 36
Woods, T. N., Eparvier, F. G., Fontenla, J., et al. 2004, Geophys. Res. Lett., 31, L10802